coatings

MDPI

Article

Enhancement of Corrosion Resistance in 304 Stainless Steel Through Hybrid Parylene C–ALD Al_2O_3 Composite Coatings

Xuewei Xie [1], Woon-Ming Lau [1], Po-Wan Shum [1,*], Yongqiang Fu [2,*] and Tao Fu [3]

[1] School of Chemistry and Chemical Engineering, Linyi University, Linyi 276000, China; maxxwell587@163.com (X.X.)
[2] School of Mechanical and Automotive Engineering, Qingdao University of Technology, Qingdao 266520, China
[3] Key Laboratory of Biomedical Information Engineering of Ministry of Education, School of Life Science and Technology, Xi'an Jiaotong University, Xi'an 710049, China
* Correspondence: shenbuyun@lyu.edu.cn (P.-W.S.); fuyongqiang@qut.edu.cn (Y.F.)

Abstract

Parylene C films are subjected to inadequate corrosion resistance due to their relatively low adhesion and structural defects. To address this challenge, the CVD Parylene C film (10 μm thick) was composited with Al_2O_3 film (30 nm thick) prepared with atomic layer deposition (ALD) technology in this work. Optical microscopic results indicate uniform thickness of the films and the reduced adhesion of Parylene C based thick films. SEM-EDX and AFM results show that the composite films have more blurred mounds morphology than the individual films, and Al_2O_3 film decreases the surface roughness of Parylene C film; compared with the single-layer film, the R_a value of the bilayer film decreased by approximately 6%. XPS, FTIR and XRD analyses confirm the structural components of Al_2O_3 and Parylene C films and the annealing effect of ALD process on Parylene C film. Tafel polarization and electrochemical impedance spectroscopy tests reveal that the 304-Parylene C–Al_2O_3 system exhibits the optimal corrosion resistance; its corrosion current density (i_{corr}) is 8.099 × 10^{-5} μA/cm^2 and the ALD Al_2O_3 thin film uniformly coats the Parylene C film, enhancing its physical barrier and chemical passivation under corrosive conditions.

Keywords: atomic layer deposition; composite film; 304 stainless steel; corrosion protection

1. Introduction

Industrially prevalent Parylene C films, with their excellent chemical inertness, low water vapor permeability, superior biocompatibility, and stability, are suitable for waterproofing and corrosion protection in devices operating in most environments [1–7]. Parylene C films adhere poorly to smooth, hydrophilic substrates due to their reliance solely on weak intermolecular interactions—namely hydrogen bonding and van der Waals forces. Consequently, delamination frequently occurs during corrosion protection, restricting their applicability in complex, harsh environments. Under the influence of water vapor permeation, the low adhesion increases the likelihood of film delamination at the interface, potentially leading to the complete loss of barrier properties—a critical flaw for long-term corrosion protection [2,8].

Atomic layer deposition (ALD) is a gas-phase thin film growth technology [9] which has unique advantages in material preparation and surface modification, such as high

Check for updates

Academic Editor: Stefano Caporali

Received: 12 January 2026
Revised: 5 February 2026
Accepted: 6 February 2026
Published: 13 February 2026

Copyright: © 2026 by the authors. Licensee MDPI, Basel, Switzerland. This article is an open access article distributed under the terms and conditions of the Creative Commons Attribution (CC BY) license.

uniformity, good conformality, precise control of composition and structure, wide application range, and the ability to achieve selective deposition. Many metallic elements, metal oxides, non-metallic elements, non-metallic oxides and many other materials can be surface modified by ALD technology [10–14]. The resulting films exhibit high density, excellent corrosion resistance, and superior water vapor barrier properties [14].

The recent works demonstrated that ALD films exhibit a certain degree of anti-permeation effect on other PVD and CVD films, in which the advantages of two coating methods are effectively combined [5,9,15–17]. The resulting composite films exhibit uniform morphology and strong interfacial adhesion to the substrate. ALD-derived films achieve near-zero defect density and conformal, complete coverage—even over complex three-dimensional topographies [18]. However, the work to fill in the defects or voids within the organic layer (e.g., Parylene C film) by ALD inorganic materials to reduce water permeability and enhance corrosion resistance has rarely been reported.

304 stainless steel is widely utilized in different industrial fields. The chromium oxide passivation layer exhibits corrosion resistance and self-healing properties [19,20]. However, under harsh service conditions—such as those encountered in high-salinity or heavily polluted industrial environments—corrosive ions can penetrate and degrade the native chromium oxide passive film, thereby initiating localized corrosion of the steel substrate [21–23]. Different films are applied to improve the anti-corrosion properties of 304 stainless steel, but single-layer PVD or CVD films are prone to form defects such as cracking and pinholes, leading to the limited effectiveness in protection against harsh environments. Moreover, increasing the thickness of inorganic films exacerbates the risk of cracking during bending, thereby restricting their applicability in flexible applications [10,24,25]. Elias et al. [11] prepared a composite film with the structure of CrN/$[Al_2O_3$-ZnO$]_n$/CrN. Compared to the single CrN film, the composite coating exhibited a hardness increment of about 2 GPa, and the corrosion current density was reduced to 7.9×10^{-10} A/cm^2. The improved structural integrity by the composite design contributes to the high corrosion resistance of the inorganic coating. Marin et al. [26] successfully fabricated a uniform, highly adherent, and defect-free bilayer coating of TiO_2/Al_2O_3 via ALD on AISI 316 stainless steel. This ALD-derived bilayer coating markedly improved the material's corrosion resistance in chloride-containing environments, suppressing the passivation current density by over two orders of magnitude. Guan et al. [7] fabricated a Parylene C/CrN bilayer coating via a hybrid chemical vapor deposition (CVD) and physical vapor deposition (PVD) approach, systematically varying the thickness of the CrN sublayer. The resulting bilayer coating exhibited a corrosion current density as low as 10^{-9} A·cm^{-2}, approximately one order of magnitude lower than that of a monolithic CrN coating. Joanna et al. [27] prepared 15 μm thick Parylene C films using EBPVD and subsequently deposited ALD films on the silicon substrate. The resulting composite films exhibited a smooth surface morphology and retained a certain flexibility. The organic based composite coatings would have better flexibility and film integrity under deformation, but the related work (e.g., Parylene C based composite films) to improve the corrosion resistance of 304 stainless steel has rarely been reported (this limited interfacial adhesion likely arises from the inherent chemical incompatibility between the organic Parylene C polymer and the metallic surface of 304 stainless steel).

In this work, CVD Parylene C–ALD Al_2O_3 composite films with a thickness of 10 μm were prepared to encapsulate the 304 stainless steel substrate (this thickness falls within the typical range employed for protective coatings in industrial packaging applications). Since ALD Al_2O_3 films demonstrated excellent corrosion resistance even at a thickness of 10 nm for stainless steel (Dinu et al. [20]), the Al_2O_3 film with the thickness of 30 nm was

prepared to composite Parylene C films. The morphology, structure and their effects on the electrochemical corrosion behaviors of the coated samples were studied.

2. Experiments

2.1. Deposition of Individual and Composite Films

A total of four sets of samples was prepared: 304–Parylene C–Al_2O_3, 304–Al_2O_3–Parylene C, and single-layer 304–Parylene C and 304–Al_2O_3 for comparison (Table 1). First, plasma cleaning of 304 stainless steel substrates (Ar purge) with a size of 15 × 15 mm^2 was performed to remove surface contaminants, followed by vacuum drying at 80 °C. Before depositing the Parylene C film, silane A-174 was coated on the substrates as an adhesion promoter. Subsequently, the Parylene C overlayer was deposited using the Gorham process (sample SP, thickness 10 μm, dichloro-[2]-paracyclophane). The thickness of 10 μm was selected as it represents the most commonly adopted value in industrial Parylene conformal coatings, providing sufficient barrier performance for standard reliability tests.

Table 1. Preparation steps for the Parylene C–Al_2O_3 film samples.

Sample	Step 1: CVD Parylene C	Step 2: ALD Al_2O_3	Step 3: CVD Parylene C
SP	Silane, 10 μm C	/	/
SA	/	30 nm Al_2O_3	/
SPA	Silane, 10 μm C	30 nm Al_2O_3	/
SAP	/	30 nm Al_2O_3	Silane, 10 μm C

Al_2O_3 films (sample SA, thickness 30 nm) were deposited by thermal ALD in a commercial reactor. A thickness of 30 nm was chosen to achieve an effective barrier while avoiding micro-crack formation, as thicker Al_2O_3 layers (>50 nm) are more prone to cracking. Trimethylaluminum (TMA, 98% purity, STREM Chemical, Newburyport, MA, USA and deionized water (Sigma-Aldrich, Burlington, MA, USA, CAS No. 7732-18-5) were used as the ALD precursors. The deposition temperature was maintained at 80 °C, and each ALD cycle required 106.8 s, corresponding to a growth rate of approximately 1.5 Å per cycle. Ultra-high-purity nitrogen was used as both the purge and carrier gas. The ALD chamber had dimensions of Φ500 mm × 500 mm. A typical ALD cycle consisted of TMA pulse time/soak time/purge time/H_2O pulse time/soak time/purge time of 0.5 s/3 s/50 s/0.3 s/3 s/50 s. After fabricating the individual films, the composite Parylene C–Al_2O_3 films SPA and SAP were deposited by combining the individual coating steps. During the deposition of the films, ellipsometry was employed for in situ monitoring to ensure the target thickness was achieved.

2.2. Characterization of Individual and Composite Films

The surface morphology and elemental composition of the coating samples were examined using a high-resolution scanning electron microscope (SEM, SEM5000, Guoyi Quantum, Hefei, Anhui, China, acceleration voltage 15 kV) equipped with an energy-dispersive X-ray spectrometer (EDS). The surface topography of the samples was analyzed by atomic force microscopy (AFM, BioScope Resolve, Bruker, Billerica, MA, USA). The elemental composition and chemical state of the Al_2O_3 thin film were analyzed using the X-ray photoelectron spectroscopy (XPS, ULVAC-PHI, Chigasaki, Kanagawa, Japan). Chemical structure analysis of the Parylene C and composite films was conducted using FTIRs (Flight Test Instrumentation Requirements) spectroscopy with the built-in ATR (attenuated total reflectance) module (Nicolet iS50ATR, Thermo-Fisher, Waltham, MA, USA). The crystal structure was characterized by X-ray diffraction (XRD, DX-2700BX, Haoyuan Instruments,

Dandong, Liaoning, China, voltage 40 kV, current 40 mA, scan range 10–90°, scan speed 10°/min, step time 0.12 s, step size 0.02°).

2.3. Electrochemical Tests

In the electrochemical corrosion tests, the Tafel polarization curves and electrochemical impedance spectroscopy (EIS) measurements were conducted. The corrosive medium was a 3.5 wt.% NaCl aqueous solution; the reference electrode was a Hg/HgO electrode, and the counter electrode was a graphite carbon electrode. Prior to each test, the open circuit potential was stabilized for 4 h and recorded to serve as the baseline reference potential. The Tafel polarization scans were performed over the potential range of −0.4 V to 0.4 V versus the open circuit potential, with a scan rate of 0.001 V/s. The samples after the polarization test were subjected to optical microscopic and SEM-EDS analyses. EIS measurements were carried out across the frequency range of 10^{-2}–10^{5} Hz, with a sinusoidal voltage perturbation with an amplitude of 0.01 V applied.

3. Results and Discussion

3.1. Morphology and Structure Analyses

The surface morphology of the prepared samples was examined by optical microscopy (Figure 1a–d). The polishing induced scratches of the steel substrate are visible, and no cracks or delamination are observed for all samples, indicating uniform thickness and good cohesion/adhesion of the films. The Parylene C film has an inherently lower density than the Al_2O_3 film. The adhesion strength between the film and substrate was quantitatively assessed via scratch testing (spherical indenter tip radius: 0.2 mm; normal load range: 1–20 N; scratch length: 10 mm). For sample SA, negligible film delamination occurred along the scratch track, indicating excellent interfacial adhesion. In contrast, samples SP, SPA, and SAP exhibited partial delamination confined to the scratch path. Notably, sample SPA showed the least extent of detachment among these three, suggesting a superior adhesion performance relative to SP and SAP, indicating the reduced adhesion of Parylene C based thick films in comparison with the Al_2O_3 thin film (insets of Figure 1a–d).

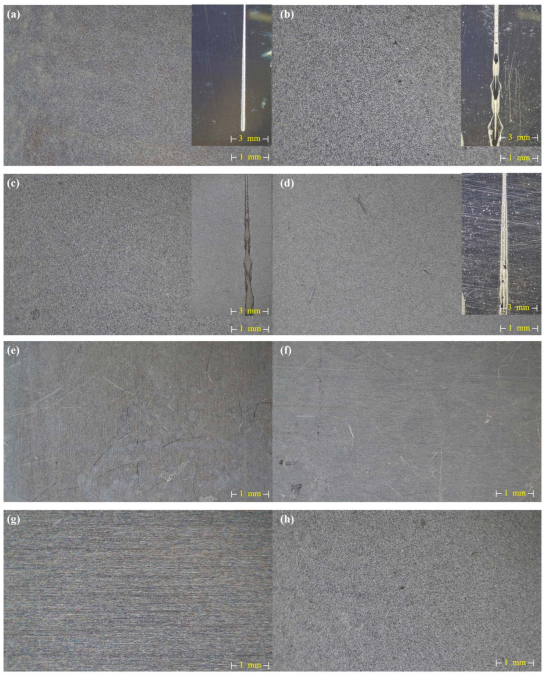


Figure 1. Optical micrographs of the film samples with the scratch images shown as the insets: (**a**) SA, (**b**) SP, (**c**) SAP, (**d**) SPA; and the samples after Tafel polarization test: (**e**) SA, (**f**) SP, (**g**) SAP, (**h**) SPA.

The surface morphology of the film samples was further examined with SEM (Figure 2). Samples SP, SAP and SPA are relatively smoother than sample SA at the surface, due to the coverage of Parylene C film on the steel substrate. The Parylene C film grew with uniform thickness, but showed mound-like morphology due to the formation of an "island" structure at the early growth stage. By comparing Figure 2c,d, the boundaries between the mounds become a little more blurred due to the deposited ALD film onto the Parylene C film. In EDS mapping the constituent elements are distributed uniformly (Figure 2). The Al signal is fairly weak for sample SAP due to the large film thickness.

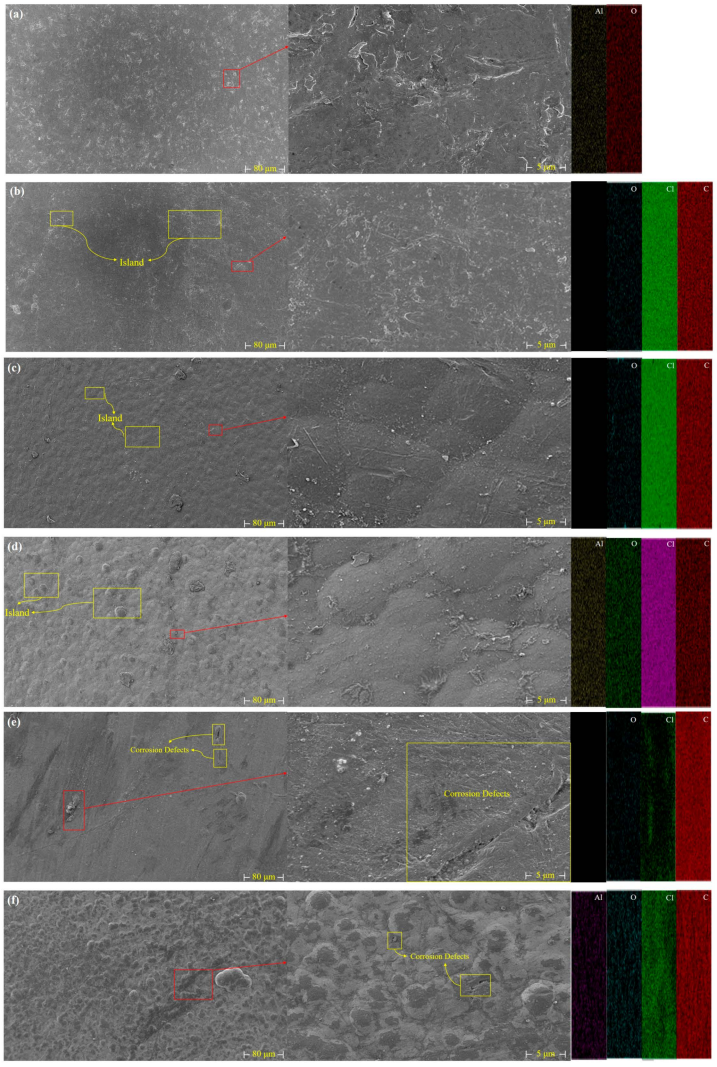


Figure 2. SEM and EDS mapping of samples, before corrosion tests: (**a**) SA; (**b**) SP; (**c**) SAP; (**d**) SPA; after Tafel polarization test: (**e**) SP; (**f**) SPA.

AFM surface images of the baseline film samples are shown in Figure 3. Surface roughness (Ra) was quantified via AFM by scanning three representative 20 × 20 µm^2 areas across the film sur-face, the mean Ra value is presented in Figure 3. The ALD Al_2O_3 film has high uniformity, but Parylene C film has trace particle aggregation. The ALD Al_2O_3 film mitigates the excessive roughness caused by these aggregated particles, as indicated by the Ra roughness and the peak–valley difference in Figure 3b,d.

XPS spectra of sample SA are shown in Figure 4. Elements of Al, O and adventitious C are detected for the 30 nm thick Al_2O_3 film. The Al 2p peak can be deconvoluted into two components [28]: the peak at 74.4 eV is attributed to Al(III) ions in the oxide matrix, while the Gaussian symmetric peak at 76.1 eV is attributed to Al(III) ions in the hydroxide

matrix. The O 1s peak is deconvoluted into two components: the one at 531.1 eV is attributed to oxygen bonded to aluminum in Al_2O_3; the other with Gaussian symmetry at 533.3 eV is attributed to oxygen from water molecules adsorbed on the surface.

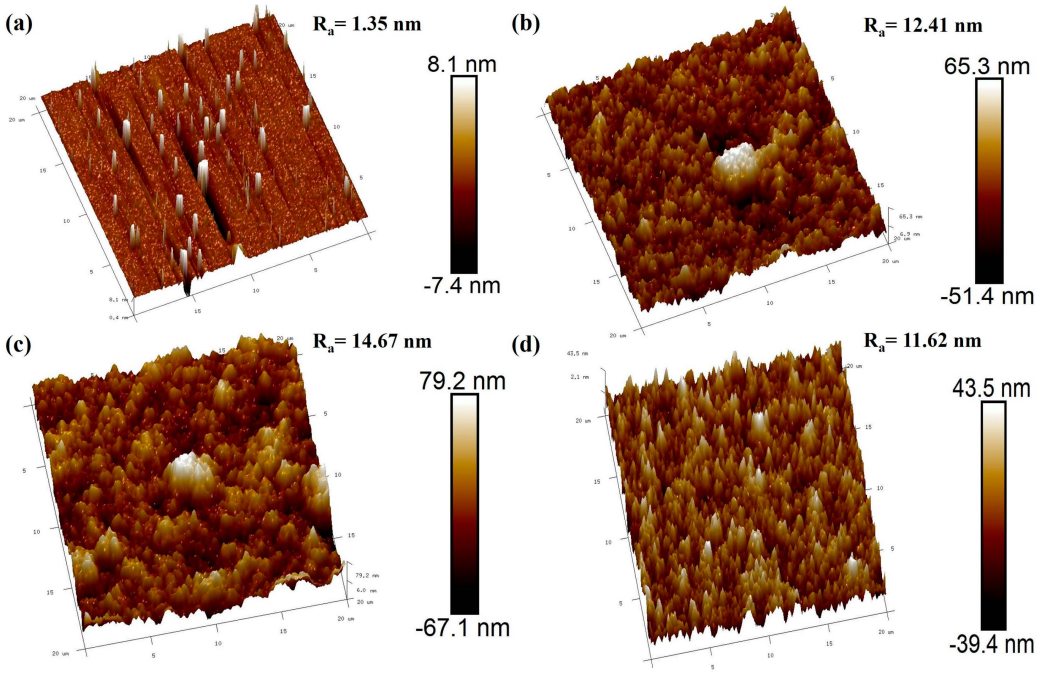


Figure 3. AFM images (20 × 20 μm^2) of samples: (**a**) SA; (**b**) SP; (**c**) SAP; (**d**) SPA.

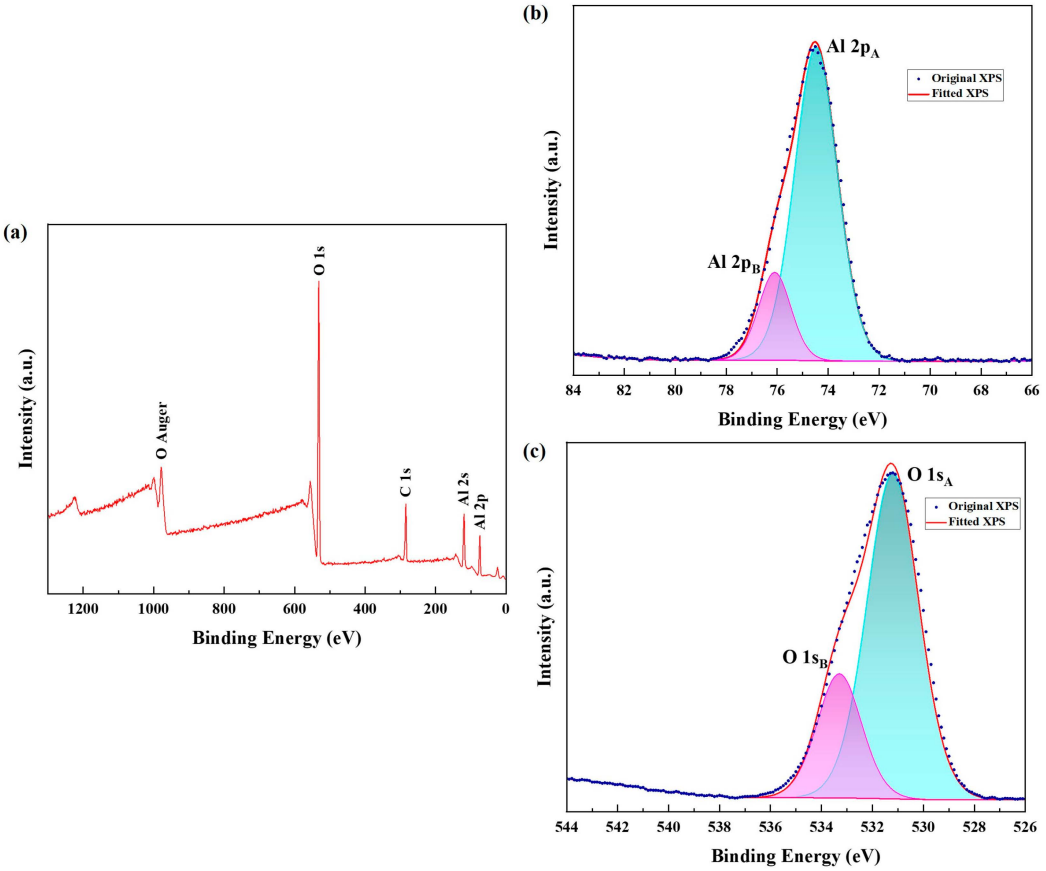


Figure 4. The XPS spectra of the ALD Al_2O_3 film (sample SA): (**a**) survey spectrum, high-resolution spectra of (**b**) Al 2p and (**c**) O 1s.

ATR-FTIR spectra of the Parylene C based film samples are shown in Figure 5. The characteristic peaks of the samples exhibit minimal difference, revealing no new peaks introduced by the ALD Al_2O_3 thin film. All samples are predominantly featured with the primary chemical bonds of Parylene C [29–31] films annealed at lower temperatures showing identical infrared spectra [32], including 2925 cm^{-1} and 2859 cm^{-1} (methylene C-H stretching vibration), 1607 cm^{-1} and 1556 cm^{-1} (aromatic backbone C-C stretching), 1493 cm^{-1} (C-C ring stretching), 1450 cm^{-1} (CH_2 bending), 1401 cm^{-1} (C-C deformation), 1208 cm^{-1}, 1156 cm^{-1} and 1105 cm^{-1} (CH_2/CH), 1048 cm^{-1}, 901 cm^{-1} and 875 cm^{-1} (C-Cl bond), and 823 cm^{-1} (single hydrogen bond on the ring with adjacent chlorine and ethyl groups).

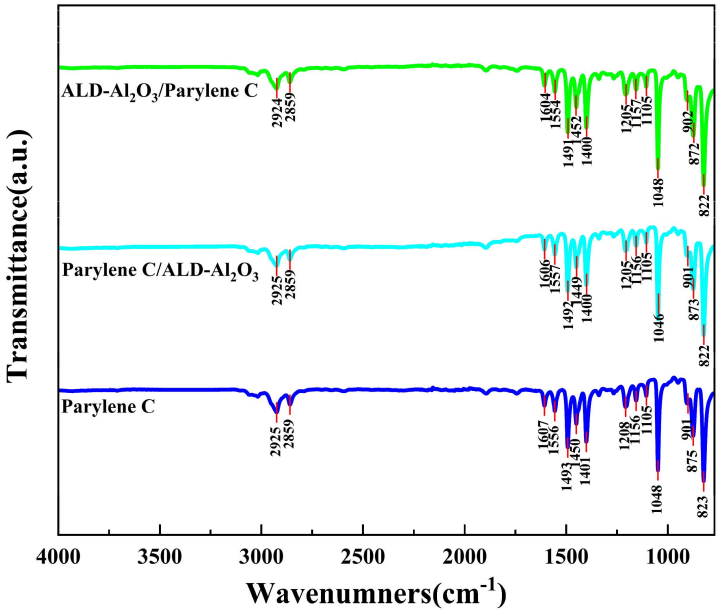


Figure 5. ATR-FTIR spectra of the Parylene C based film samples.

XRD spectra of the film samples are shown in Figure 6. During the process of depositing Parylene C, different deposition processes introduce compressive stress, forcing the rearrangement of the Parylene C molecular chains into a more crystalline structure [8,17], resulting in sharper diffraction peaks. The diffraction peaks of Parylene C in sample SPA appear sharper than those in individual Parylene C sample SP [8,17], and FWHM (full width at half maxima) is 0.82° (SPA) and 0.92° (SP), respectively.

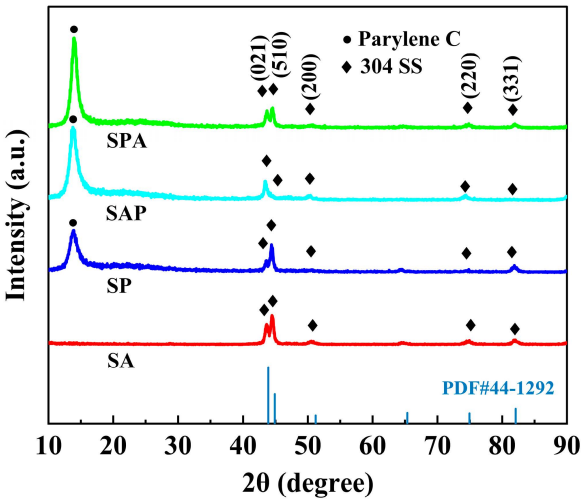


Figure 6. XRD patterns of the film samples.

3.2. Tafel Polarization Test Results

Since the passivation layer of 304 stainless steel is vulnerable to chloride ions, the moderately corrosive 3.5 wt.% NaCl solution was selected as the test medium. The Tafel polarization curves are shown in Figure 7, and the corrosion potential (E_{corr}) and corrosion current density (i_{corr}) are listed in Table 2. Mechanical polishing of the 304 stainless steel substrate inevitably introduces surface imperfections—including scratches—which contribute to the observed variation in corrosion potential (E_{corr}) among the samples. The results reveal that all film samples have a significantly increased corrosion potential and a decreased corrosion current density than the 304SS sample; this demonstrates that the films significantly suppressed the corrosion reactions on the sample surfaces, thereby markedly improving their corrosion resistance.

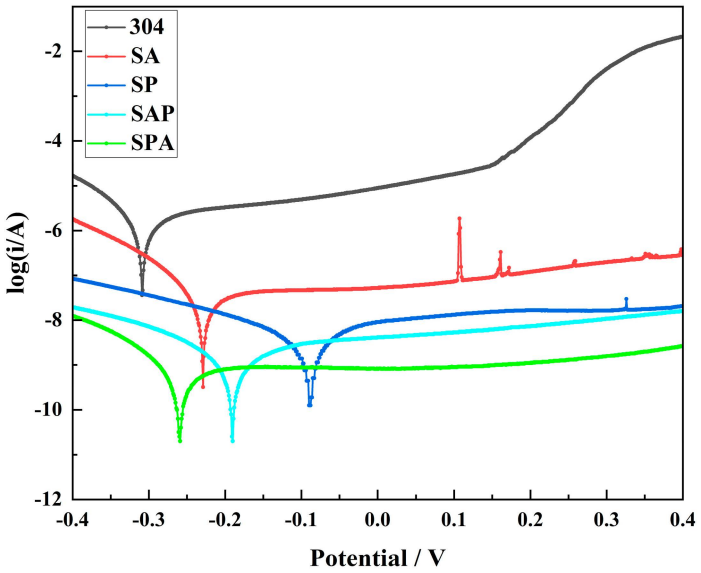


Figure 7. Tafel polarization curves of the samples.

Table 2. Corrosion potential and corrosion current density of the samples.

Sample	E_{corr} (V)	i_{corr} (μA/cm^2)
304	−0.3089	3.878×10^{-1}
SA	−0.2292	3.938×10^{-3}
SP	−0.0927	6.727×10^{-4}
SAP	−0.1911	1.380×10^{-4}
SPA	−0.2593	8.099×10^{-5}

Sample SA has a dense and highly conformal Al_2O_3 film with a strong electrochemical shielding effect that can effectively block electron transport pathways in the corrosion reaction. The inherent chemical inertness of the Al_2O_3 film provides effective resistance against Cl^- ion attacks [33]. Sharma et al. [25] conducted electrochemical corrosion testing on ALD Al_2O_3 films at varying anodic potentials and temperatures, concluding that the films maintained high polarization resistance even at high potentials of 0.7 V and elevated temperatures of 60 °C. Dinu et al. [24] comprehensively evaluated the relationship between the thickness and corrosion resistance of common ALD films, Al_2O_3, ZrO_2, and HfO_2, among which Al_2O_3 films demonstrated the best performance, maintaining excellent corrosion resistance even at a thickness of 10 nm.

For sample SP, the Parylene C film also has a physical barrier effect; it has a greater film thickness, and the longer penetration path for Cl^- ions makes the migration in the corrosive medium more challenging. Therefore, sample SP has a smaller i_{corr} value than

sample SA. In the optical and SEM micrographs, distinct corrosion marks (Figure 1e,f and Figure 2e,f) are observed for samples SA and SP after the corrosion test. Sample SP has higher densities of pitting and defects than sample SA, due to the inherently lower density and adhesion of the Parylene C film than the Al_2O_3 film (Figure 1a,b).

Sample SAP has a much smaller i_{corr} value than sample SP, which can be attributed to the strong interfacial bonding [14], high uniformity, and good conformality of the ALD Al_2O_3 film as the interlayer. In the corrosion test of the SAP sample, even the corrosive medium penetrates the Parylene C outer layer, the inner Al_2O_3 layer can block the transmission of Cl^- ions, and the reactions at the film/substrate interface are prevented.

Sample SPA with the ALD Al_2O_3 outer layer has an even smaller i_{corr} value (8.099×10^{-5} μA/cm^2) than sample SAP with the Parylene C outer layer. In the optical micrographs (Figure 1g,h), samples SAP and SPA still maintain their initial uniform morphology.

By SEM observation of the corroded samples SP and SPA (Figure 2e,f), the corrosion effects of two different structural films on 304 steel were compared. Sample SP exhibits distinct pitting corrosion, manifested as elongated corrosion defects. In contrast, no specific pitting corrosion was observed for sample SPA at a low magnification, and only minute defects are visible at a high magnification. The EDS mapping images indicate that the intensity of the Cl element in the Parylene C film of sample SP is obviously reduced after corrosion (Figure 2b,e), while the intensities of Cl and Al elements in the composite film of sample SPA remain nearly unchanged after corrosion (Figure 2d,f). This indicates that the Al_2O_3 film provides good protection for the Parylene C film.

3.3. EIS Test Results

Electrochemical impedance spectra of the samples are shown in Figure 8. The Nyquist plots exhibit near-semicircular characteristics (Figure 8a,b). With the increases in film thickness, the curvature radius of the plots is greatly increased.

In Bode modulus plots, the higher magnitude corresponds to the higher corrosion resistance. As shown in Figure 8c, the magnitude follows the order SA < SP < SAP < SPA, demonstrating that the SPA composite film exhibits the highest corrosion resistance among all samples.

The Bode phase angle plot (Figure 8d) shows that all coated samples—except SP—exhibit consistently high phase angles across the entire measured frequency range, with particularly pronounced values in the mid-frequency region. This sustained phase angle elevation reflects the robust capacitive behavior and exceptional stability of the protective barrier, indicative of superior and durable corrosion resistance. In contrast, sample SP displays a marked decline in the phase angle at low frequencies, signaling the onset of localized breakdown and progressive electrolyte penetration, consistent with the severe corrosion induced by prolonged exposure to the aggressive medium. This corroborates that Parylene films are prone to delamination at the interface after prolonged immersion in corrosive media [2]. In Bode plots, the higher Z values at lower frequencies indicate superior corrosion resistance.

Two equivalent circuits in Figure 8e,f were used to simulate the EIS results, in which R_s represents the solution resistance. Due to the short immersion time (prior to initiating the experiment, this work observed that organic films exhibit greater difficulty in adapting to inorganic corrosive environments [2,8]; to ensure sample stability in corrosive media, all samples were subjected to a salt spray environment for 4 h prior to open circuit potential measurements), the model for the 304 steel sample consists of the phase angle element Q_{dl} in parallel with the charge transfer resistance R_{ct}. For the film samples, the addition of films introduces another long phase angle element Q_c and the film resistance R_c, effectively

preventing direct contact between the 304 substrate and the corrosive medium. The capacitive phase element (Q) has an exponent of n, representing the deviation from the ideal capacitance (n = 0–1).

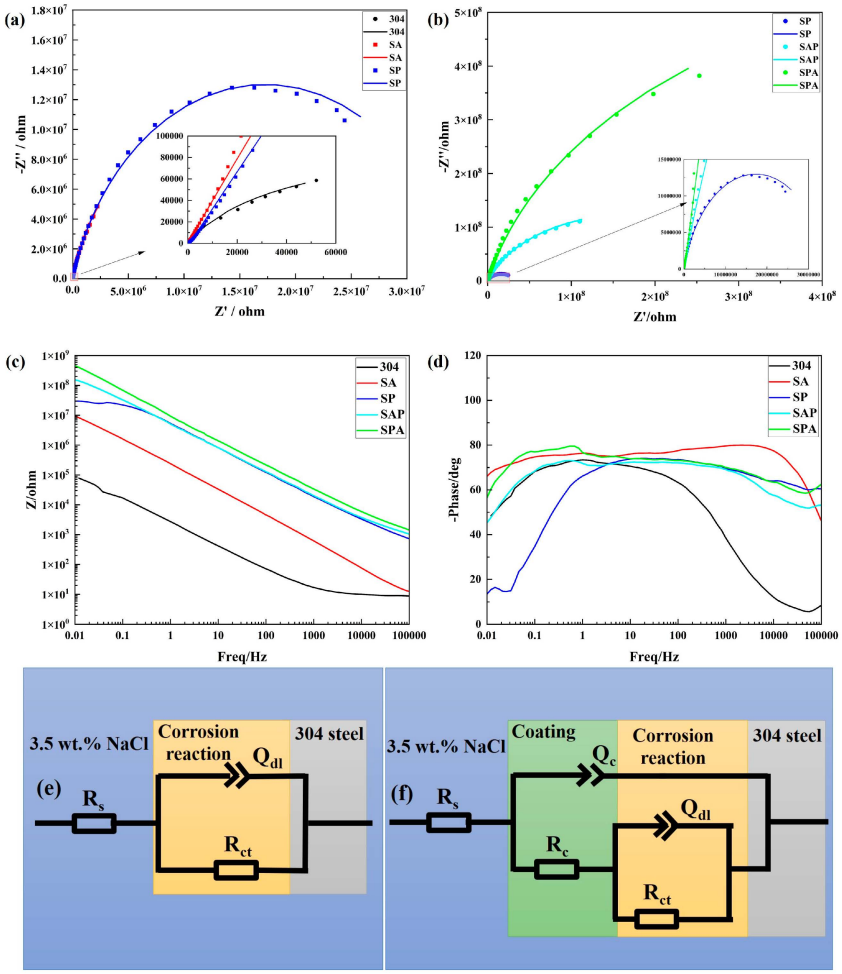


Figure 8. EIS Nyquist plots (**a**,**b**), Bode plots (**c**,**d**), and the equivalent circuit used for simulating the data of (**e**) bare 304 steel sample and (**f**) film samples.

The EIS fitting results are presented as scatter plots in Figure 8a,b, with the corresponding equivalent circuit component parameters summarized in Table 3. As is evident from the fitted data, all film-coated samples exhibit significantly higher polarization resistance R_{ct}—a key indicator of corrosion resistance—compared to the bare 304 stainless steel substrate (R_{ct}(304): 3.579 × 10^4 Ω·cm^2, R_{ct}(SA): 8.055 × 10^7 Ω·cm^2). The R_{ct} values are increased for film samples due to the large thickness and superior protective performance of Parylene C based films, with the order of R_{ct}(SA) < R_{ct}(SP) < R_{ct}(SAP) < R_{ct}(SPA). Notably, the R_{ct} value of sample SPA is very high (1930 MΩ·cm^2), indicating its superior corrosion resistance. The R_c value is determined by the number of micro-pores at the film surface and the number of internal film channels, thereby directly governing the penetrating rate of the corrosive media toward the substrate surface [10,34]. In Table 3, sample SPA exhibits the highest R_c value (3657 Ω·cm^2), consistent with the results from Tafel polarization curve analysis.

The advantage of sample SPA lies in its lower surface roughness compared to samples SP and SAP (Figure 3). The main component of Parylene C remains essentially unchanged (Figure 5). Moreover, it exhibits excellent resistance to electrochemical corrosion (Figures 5 and 6).

Table 3. Component parameters obtained by fitting the EIS data (Figure 8a–d) with the equivalent circuits shown in Figure 8e,f, respectively.

Sample	R_s ($\Omega \cdot cm^2$)	R_c ($\Omega \cdot cm^2$)	R_{ct} ($\Omega \cdot cm^2$)	Q_c ($F \cdot cm^{-2}$)	n-Q_c	Q_{dl} ($F \cdot cm^{-2}$)	n-Q_{dl}	Chsq (10^{-3})
304	7.55	/	3.579×10^4	/	/	7.645×10^{-5}	0.887	2.539
SA	4.94	5.7	8.055×10^7	1.316×10^{-3}	0.994	7.968×10^{-7}	0.801	0.451
SP	34.37	690.6	1.343×10^8	1.882×10^{-8}	0.865	3.967×10^{-8}	0.822	7.747
SAP	53.64	2798.0	3.306×10^8	1.571×10^{-8}	0.812	2.747×10^{-8}	0.805	0.533
SPA	64.55	3657.0	1.930×10^9	3.013×10^{-8}	0.836	2.117×10^{-8}	0.840	6.115

Numerous studies have demonstrated that when ALD films are deposited onto other PVD and CVD thin films, the resultant composite coatings exhibit long-term corrosion resistance due to the effective sealing effect of ALD layers [35–37]. M Staszuk et al. [38] reported that the ALD-grown TiO_xN_y–TiN layer confers superior corrosion protection to CrN films deposited on stainless steel substrates. Similarly, the present work shows that the ALD Al_2O_3 outer layer has markedly improved the corrosion resistance of Parylene C-coated 304 stainless steel. The exceptional corrosion resistance exhibited by sample SPA is attributed to the composite film's superior physical barrier properties and effective chemical passivation capability, as substantiated by its remarkably high R_c value in the electrochemical impedance spectroscopy (EIS) measurements. This finding suggests the following hypothesis for further consideration: the organic Parylene C film with molecular chain voids allows the TMA precursor to diffuse into the film matrix during the Al_2O_3 film deposition. The TMA molecules are then kinetically captured by the polymer chains, resulting in a dense and uniform composite film structure and enhanced physical barrier properties in corrosion tests. Additionally, based on the highest R_{ct} value derived from fitting the results in Table 3, it can be concluded that the Parylene C composite film in the SPA sample exhibits the most pronounced inhibitory effect on the corrosion reaction. This is attributable to the high surface density of the film [13,36], which effectively impedes the penetration of corrosive species.

4. Conclusions

The Parylene C–ALD Al_2O_3 composite films and the individual films were deposited on 304 stainless steel substrates. The Parylene C–ALD Al_2O_3 composite films demonstrate excellent thickness uniformity and robust interfacial adhesion to the substrate. The composite films have more blurred mounds morphology than the individual Parylene C and Al_2O_3 films, and the Al_2O_3 film decreases the surface roughness of the Parylene C film. The coated samples exhibit an increased corrosion potential, decreased corrosion current density and larger charge transfer resistance compared with the polished 304 steel samples in the Tafel polarization and electrochemical impedance spectroscopy tests. The 304–Parylene C–Al_2O_3 system exhibits a significantly enhanced corrosion resistance, demonstrating its capacity to provide robust, short-term protective coverage for the 304 stainless steel substrate under corrosive conditions.

Author Contributions: Writing—original draft, X.X.; Writing—review & editing, P.-W.S. and Y.F.; Visualization, W.-M.L.; Supervision, T.F. All authors have read and agreed to the published version of the manuscript.

Funding: Shandong Provincial Higher Education Youth Innovation Team Program (2023KJ116).

Institutional Review Board Statement: Not applicable.

Informed Consent Statement: Not applicable.

Data Availability Statement: The original contributions presented in this study are included in the article. Further inquiries can be directed to the corresponding authors.

Conflicts of Interest: The authors declare no conflict of interest.

References

1. Hsu, J.-M.; Rieth, L.; Normann, R.A.; Tathireddy, P.; Solzbacher, F. Encapsulation of an integrated neural interface device with Parylene C. *IEEE Trans. Biomed. Eng.* **2008**, *56*, 23–29. [CrossRef]
2. Li, W.; Rodger, D.; Menon, P.; Tai, Y.-C. Corrosion behavior of parylene-metal-parylene thin films in saline. *ECS Trans.* **2008**, *11*, 1. [CrossRef]
3. Gorham, W.F. A new, general synthetic method for the preparation of linear poly-p-xylylenes. *J. Polym. Sci. Part A-1 Polym. Chem.* **1966**, *4*, 3027–3039. [CrossRef]
4. Kahouli, A. Effect of film thickness on structural, morphology, dielectric and electrical properties of parylene C films. *J. Appl. Phys.* **2012**, *112*, 064103. [CrossRef]
5. Cieślik, M.; Engvall, K.; Pan, J.; Kotarba, A. Silane–parylene coating for improving corrosion resistance of stainless steel 316L implant material. *Corros. Sci.* **2011**, *53*, 296–301. [CrossRef]
6. Chung, C.-H.; Kuo, W.-C. Anti-corrosion application of parylene C film for stainless steel fasteners in electroplating industry. *AIP Adv.* **2024**, *14*, 035250. [CrossRef]
7. Guan, X.; Cui, S.; Cao, Y.; Zhang, L. New coating with superior corrosion and wear performances: Parylene C/CrN duplex coating. *J. Vac. Sci. Technol. B* **2023**, *41*, 064003. [CrossRef]
8. Chen, Z.; Jin, Y.; Yin, X.; Chen, Y.; Liu, Y.; Ying, H.; Yang, W. Self-doped poly(aniline-co-metanilic acid) copolymer coatings for enhancing the corrosion resistance of 304 stainless steel. *Thin Solid Films* **2022**, *761*, 139524. [CrossRef]
9. Chai, Z.; Liu, Y.; Li, J.; Lu, X.; He, D. Ultra-thin Al_2O_3 films grown by atomic layer deposition for corrosion protection of copper. *RSC Adv.* **2014**, *4*, 50503–50509. [CrossRef]
10. Jiao, Z.-J.; Yu, C.; Wang, X.-M.; Zhou, Y.-F.; Guo, L.; Xia, Y.; Zhang, B.-C.; Zeng, R.-C. Corrosion resistance enhanced by an atomic layer deposited Al_2O_3/micro-arc oxidation coating on magnesium alloy AZ31. *Ceram. Int.* **2024**, *50*, 5541–5551. [CrossRef]
11. Kaady, E.; Alhussein, A.; Bechelany, M.; Habchi, R. Al_2O_3-ZnO atomic layer deposited nanolaminates for improving mechanical and corrosion properties of sputtered CrN coatings. *Thin Solid Films* **2022**, *759*, 139476. [CrossRef]
12. George, S.M. Atomic layer deposition: An overview. *Chem. Rev.* **2010**, *110*, 111–131. [CrossRef] [PubMed]
13. Marin, E.; Lanzutti, A.; Guzman, L.; Fedrizzi, L. Chemical and mechanical characterization of thermal-multilayered Al_2O_3 atomic layer depositions on AISI 316L stainless steel. *Metallogr. Microstruct. Anal.* **2013**, *2*, 313–320. [CrossRef]
14. Santinacci, L. Atomic layer deposition: An efficient tool for corrosion protection. *Curr. Opin. Colloid Interface Sci.* **2023**, *63*, 101674. [CrossRef]
15. Staszuk, M.; Pakuła, D.; Reimann, Ł.; Kloc-Ptaszna, A.; Lukaszkowicz, K. Structure and properties of the TiN/ZnO coating obtained by the hybrid method combining PVD and ALD technologies on austenitic Cr-Ni-Mo steel substrate. *Surf. Interfaces* **2023**, *37*, 102693. [CrossRef]
16. Alias, R.; Mahmoodian, R.; Genasan, K.; Vellasamy, K.M.; Hamdi Abd Shukor, M.; Kamarul, T. Mechanical, antibacterial, and biocompatibility mechanism of PVD grown silver–tantalum-oxide-based nanostructured thin film on stainless steel 316L for surgical applications. *Mater. Sci. Eng. C* **2020**, *107*, 110304. [CrossRef]
17. Wang, J.; Wang, Z.; Wu, R.; Zhang, X.; Luo, W.; Wang, L.; Wang, J. Study on the corrosion resistance of KH570 modified titanium oxide coating synthesized at low temperature on 304 stainless steel. *Mater. Chem. Phys.* **2025**, *329*, 130126. [CrossRef]
18. Willis, S.A.; McGuinness, E.K.; Li, Y.; Losego, M.D. Re-examination of the Aqueous Stability of Atomic Layer Deposited (ALD) Amorphous Alumina (Al_2O_3) Thin Films and the Use of a Postdeposition Air Plasma Anneal to Enhance Stability. *Langmuir* **2021**, *37*, 14509–14519. [CrossRef]
19. Anderson, M.D.; Aitchison, B.; Johnson, D.C. Corrosion Resistance of Atomic Layer Deposition-Generated Amorphous Thin Films. *ACS Appl. Mater. Interfaces* **2016**, *8*, 30644–30648. [CrossRef]
20. Daubert, J.S.; Hill, G.T.; Gotsch, H.N.; Gremaud, A.P.; Ovental, J.S.; Williams, P.S.; Oldham, C.J.; Parsons, G.N. Corrosion Protection of Copper Using Al_2O_3, TiO_2, ZnO, HfO_2, and ZrO_2 Atomic Layer Deposition. *ACS Appl. Mater. Interfaces* **2017**, *9*, 4192–4201. [CrossRef] [PubMed]
21. Bateni, M.R.; Szpunar, J.; Wang, X.; Li, D. Wear and corrosion wear of medium carbon steel and 304 stainless steel. *Wear* **2006**, *260*, 116–122. [CrossRef]
22. Zheng, Z.B.; Zheng, Y.G. Effects of surface treatments on the corrosion and erosion-corrosion of 304 stainless steel in 3.5% NaCl solution. *Corros. Sci.* **2016**, *112*, 657–668. [CrossRef]
23. Corrosion and Environmental Degradation, Volumes I & II (Book Review). *Anti-Corros. Methods Mater.* **2000**, *47*. [CrossRef]
24. Dinu, M.; Wang, K.; Mouele, E.S.M.; Parau, A.C.; Vladescu, A.; Liang, X.; Braic, V.; Petrik, L.F.; Braic, M. Effects of Film Thickness of ALD-Deposited Al_2O_3, ZrO_2 and HfO_2 Nano-Layers on the Corrosion Resistance of Ti(N,O)-Coated Stainless Steel. *Materials* **2023**, *16*, 2007. [CrossRef]
25. Sharma, A.; Manna, S.; Mishra, P.K.; Singh, S.; Satpati, A.K. Stabilization of the stainless-steel interface using sequentially deposited Al_2O_3 nano films using atomic layer deposition (ALD) technique. *Surf. Sci. Technol.* **2024**, *2*, 21. [CrossRef]

26. Marin, E.; Lanzutti, A.; Guzman, L.; Fedrizzi, L. Corrosion protection of AISI 316 stainless steel by ALD alumina/titania nanometric coatings. *J. Coat. Technol. Res.* **2011**, *8*, 655–659. [CrossRef]
27. Njeim, J.; Alamarguy, D.; Tu, X.; Durnez, A.; Lafosse, X.; Chretien, P.; Madouri, A.; Ren, Z.; Brunel, D. Effect of the Al_2O_3 Deposition Method on Parylene C: Highlights on a Nanopillar-Shaped Surface. *ACS Omega* **2020**, *5*, 15828–15834. [CrossRef]
28. Díaz, B.; Härkönen, E.; Światowska, J.; Maurice, V.; Seyeux, A.; Marcus, P.; Ritala, M. Low-temperature atomic layer deposition of Al_2O_3 thin coatings for corrosion protection of steel: Surface and electrochemical analysis. *Corros. Sci.* **2011**, *53*, 2168–2175. [CrossRef]
29. Nowlin, T.; Smith, D.F., Jr.; Cieloszyk, G. Thermal oxidative stability of poly-p-xylylenes. *J. Polym. Sci. Polym. Chem. Ed.* **1980**, *18*, 2103–2119. [CrossRef]
30. Herman, M.J.; Blair, M.W. Determination of chemical decay mechanisms of Parylene-C during X-ray irradiation using two-dimensional correlation FTIR. *Polym. Degrad. Stab.* **2020**, *171*, 109024. [CrossRef]
31. Caldwell, R.; Street, M.G.; Sharma, R.; Takmakov, P.; Baker, B.; Rieth, L. Characterization of Parylene-C degradation mechanisms: In vitro reactive accelerated aging model compared to multiyear in vivo implantation. *Biomaterials* **2020**, *232*, 119731. [CrossRef]
32. von Metzen, R.P.; Stieglitz, T. The effects of annealing on mechanical, chemical, and physical properties and structural stability of Parylene C. *Biomed. Microdevices* **2013**, *15*, 727–735. [CrossRef] [PubMed]
33. Lu, Y.; Chen, Z.; Wang, C.; Zhao, Q.; Zhang, K.; Du, Y.; Xin, L.; Zhu, S.; Wang, F. Protection of 304 stainless steel by nano-modified silicone coating in cyclically alternate corrosion environment. *Corros. Sci.* **2021**, *190*, 109712. [CrossRef]
34. Oliveira, M.P.; Silva, R.M.; Yasakau, K.A.; Bastos, A.; Kallip, S.; Zheludkevich, M.L.; Silva, R.F.; Ferreira, M.G.S. Atomic layer deposition of nanometric alumina for corrosion protection of heterogeneous metallic surfaces—The case of aeronautical grade aluminium alloy 2024-T3. *Corros. Sci.* **2022**, *209*, 110773. [CrossRef]
35. Marin, E.; Guzman, L.; Lanzutti, A.; Fedrizzi, L.; Saikkonen, M. Chemical and electrochemical characterization of hybrid PVD+ALD hard coatings on tool steel. *Electrochem. Commun.* **2009**, *11*, 2060–2063. [CrossRef]
36. Gong, N.; Seet, H.; Cao, J.; Luai Meng, T.; Wang, Y.; Tan, D.C.C.; Kiang Ivan Tan, C.; Suwardi, A.; Zhu, Q.; Blackwood, D.J.; et al. Atomic layer deposition of Al_2O_3 thin films for corrosion protections of additive manufactured and wrought stainless steels 316L. *Mater. Lett.* **2023**, *331*, 133434. [CrossRef]
37. Bahari, H.S.; Savaloni, H. Surface analysis of Cu coated with ALD Al_2O_3 and its corrosion protection enhancement in NaCl solution: EIS and polarization. *Mater. Res. Express* **2019**, *6*, 086570. [CrossRef]
38. Staszuk, M.; Reimann, Ł.; Pakuła, D.; Pawlyta, M.; Musztyfaga-Staszuk, M.; Czaja, P.; Beneš, P. Investigations of TiO_2/NanoTiO_2 Bimodal Coatings Obtained by a Hybrid PVD/ALD Method on Al-Si-Cu Alloy Substrate. *Coatings* **2022**, *12*, 338. [CrossRef]

Disclaimer/Publisher's Note: The statements, opinions and data contained in all publications are solely those of the individual author(s) and contributor(s) and not of MDPI and/or the editor(s). MDPI and/or the editor(s) disclaim responsibility for any injury to people or property resulting from any ideas, methods, instructions or products referred to in the content.